Innovative Mode Enhancement for High Power Coaxial Vircators

Lorenzo Valletti, Stefano Fantauzzi, and Franco Di Paolo, *Member, IEEE*

***Abstract*— The size and weight of a high power microwave (HPM) source can make a difference in strategic use. The compactness of the virtual cathode oscillator (vircator) is undoubtedly the most significant advantage of this device. Civil industry and agriculture can use it to treat objects, food, and soils for disinfestation and disinfection. Vircators could also generate electromagnetic pulses (EMPs) to force the arrest of vehicles and drones; EMPs could inhibit or activate improvised explosive devices (IEDs). The coaxial type vircator is a highly compact device. Due to its symmetric geometry, coaxial vircator is typically designed to work with a TM_{01} mode. Still, when radiated into space, this mode gives maximum RF energy away from the antenna axis, a situation not desired. Instead, the TE_{11} is convenient in applications involving precise antenna pointing since this mode gives a maximum RF energy precisely aligned to the antenna axis. By studying Mathieu functions applied to elliptical waveguides, we improve the performances of a TE_{11} mode coaxial vircator using an elliptic drift tube (EDT). This is a completely innovative solution to reduce the mode competition inside the coaxial vircator. The rms and peak output power efficiency of the EDT coaxial vircator were measured on the TE_{11} mode, obtaining the values of 6.1% and 10%, respectively, with a peak power of 450 MW in a highly compact device.**

***Index Terms*— Anode characterization, elliptical waveguide, high efficiency, high power microwave (HPM), Mathieu functions, virtual cathode oscillator (vircator).**

I. Introduction

MANY military and civil areas require a radio frequency power of hundreds of megawatts. High power microwave (HPM) vacuum tube devices can generate this power, but they are often huge and impractical in areas with limited space. One field of use for such devices is to generate strong electromagnetic fields to intentionally disturb or destroy electronic equipment without damaging infrastructure or injuring people. Considering solid-state devices, recent advances in GaN technology allow us to obtain solid-state high power amplifiers (SSHPAs) at high frequencies and with high reliability [1]. Spatial power amplifiers (SPAs) [2], [3], [4], [5], [6], [7] are the most desired SSHPA-based devices whenever small size, solid-state high-power density, and graceful degradation are needed. The examples of application fields are strategic electronic warfare (EW), electronic counter measurement/electronic counter counter measurements (ECM/ECCMs) systems, and space communications applications. With actual solid-state devices' available RF output power, a single SPA is confined to some kilowatt output power levels at the X-band, even less for higher operating frequencies. However, considering the output power as the only important aspect of power amplifiers, the vacuum tube technology has leadership since extremely high RF powers can be reached, especially for pulsed applications [8]. GW-class pulsed-type devices reduce the space occupied and increase the mechanical design simplicity. Electromagnetic pulses (EMPs) generated by these devices can neutralize systems based on solid-state devices. There are two outcomes of an HPM EMP: hard kill and soft kill; in the first case, the target is irreparably damaged, while in the second case, there are temporary malfunctions, such as making the target unusable. Applying countermeasures to avoid an EMP attack, such as shielding the target, is possible. However, a hard kill attack can act rigorously on all the most exposed systems, such as power supply wiring, remote control, and front ends. HPM EMP can be used for the forced arrest of vehicles and drones by civil and military authorities and the inhibition or activation of improvised explosive devices (IEDs) [9], [10], [11].

In civil industry and agriculture, it is possible to use HMP devices to treat objects, food, and soils for disinfestation and disinfection [12], [13].

Many HPM devices are currently huge due to the use of heavy and bulky components present in the devices in use, such as the large electromagnets of the magnetron [14] or the klystron [15] or the large dimensions of the structures that make up the gyrotron. The virtual cathode oscillator (vircator) is an excellent candidate among HPM devices due to its compactness and the absence of a bulky external magnetic field generator, resulting in a remarkable power density. The vircator is a device capable of providing GW of pulsed power for frequencies below 10 GHz: the efficiency is, however, low, and reliable values are settled on 5%–15% [16], [17], [18]. In some simulations, efficiency is higher, using reflectors and multibeam techniques [19], [20], [21]. The compactness of the vircator, with the same output power as other devices, is undoubtedly the most significant advantage of this device.

Manuscript received 2 March 2023; revised 29 April 2023; accepted 4 May 2023. Date of publication 18 May 2023; date of current version 21 June 2023. The review of this article was arranged by Editor S. Prasad. *(Corresponding author: Lorenzo Valletti.)*

The authors are with the Department of Electronic Engineering, University of Rome "Tor Vergata," 00133 Rome, Italy (e-mail: lorenzo.valletti@uniroma2.it).

Color versions of one or more figures in this article are available at https://doi.org/10.1109/TED.2023.3274497.

Digital Object Identifier 10.1109/TED.2023.3274497

There are many types of vircators [22] and different geometries; the most compact and performing vircator we have studied is the coaxial vircator. Its radial symmetry allows it to obtain a higher power with the same space as the other vircators. The coaxial vircator usually works with the TM_{01} mode, mainly excited by its inherent symmetry; the performances obtained on a coaxial vircator optimized for the TM_{01} mode are shown in [22]. However, by modifying the geometry of the coaxial vircator, it is possible to obtain other modes than the TM_{01}. The TM_{01} mode is not suitable for precise antenna-focusing applications. An antenna usually used with HPMs is the horn. It is possible to use mode transformers, which could have losses and worsen the output matching. In this work, we optimized a coaxial vircator for the TE_{11} mode enhancement, modifying the geometry of the emitter, the anode, and the output waveguide, exploiting the properties of elliptical waveguides. This is a completely innovative solution to reduce the mode competition inside the coaxial vircator, starting from a device with a feasible efficiency. To the best of our knowledge, it is the first time that such an approach for TE_{11} mode enhancement has been presented in the literature.

This article is organized as follows. In Section II, the design of a TM_{01} coaxial vircator will be presented. In Section III, we will show the optimization of the coaxial vircator for the TE_{11} mode. In Sections IV and V, we will describe the studies on elliptical waveguides and their use on the TE_{11} coaxial vircator.

II. Coaxial Vircator Design

The coaxial-type vircator is a device that exploits the radial symmetry in all the components. The anode, emitter, and output waveguide develop as coaxial cylinders along the direction of field propagation. The output waveguide is also called drift tube (DT). We designed the device with the 2-D theoretical models [23] and then simulated and optimized it with the full 3-D particle-in-cell (PIC) software CST Studio Suite. In devices with applied voltage (V_0) not exceeding 500 kV, the dominant frequency can be derived from the following equation, which is valid for nonrelativistic working conditions:

$$f_d \approx 9.44 \times 10^4 \cdot \frac{(R_a/R_c)^{(1/4)}}{R_a - R_c} V_0^{1/2}. \quad (1)$$

In the designed structure, the anode is a section of DT semi-permeable to electrons, with a sheet transparency of 80% [22], [24], [25], while the emitter is a section of the cathode cylinder; R_a is the radius of the DT and the anode, and R_c is the radius of the cathode and the emitter. The external cavity guarantees the vacuum and the matching. Fig. 1 shows the described structure.

The voltage (V_0) stimulus used is a 350-kV pulse, with a duration of 50 ns and a rise time of 10 ns. The instantaneous distribution of the particles is shown in Fig. 2; the accumulation of quasi-static charges in the center of the DT (blue zone) shows the presence of a virtual cathode [22]. The signal power in the time domain on the RF output port is shown in Fig. 3, and the spectral power density is shown in Fig. 4.

Fig. 5 shows the normalized y-component of the electric field at 2.45 GHz; the E-field distribution confirms the predominance of TM_{01}. The average power and the efficiency were calculated from the rms value considering all the pulse duration. An rms power efficiency of 6.8% was obtained for the pulse duration, consistent with values found in the literature [18], [26], [27].

Fig. 6 shows the negligible power of the TE_{11} mode: with an rms efficiency less than 0.01%. Table I shows the obtained values of the optimized coaxial vircator.

Ignoring the space occupied by the primary source, e.g., the Marx generator [28], [29], [30], [31], which depends

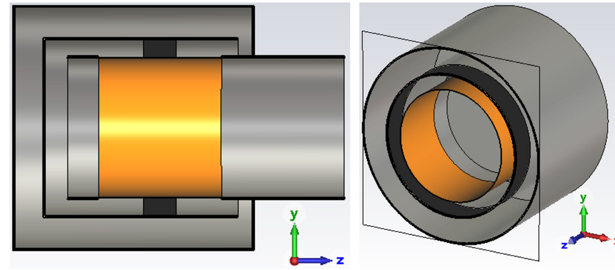

Fig. 1. Coaxial vircator: longitudinal and transversal section.

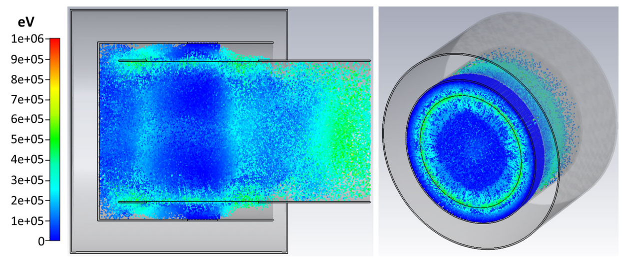

Fig. 2. Instantaneous distribution of the electrons during the pulse.

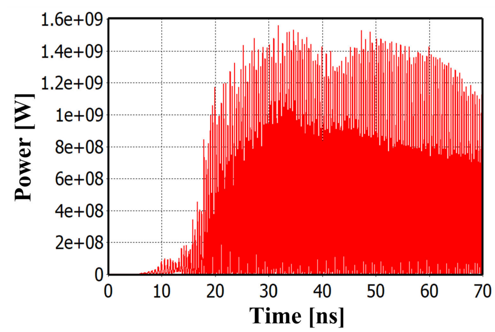

Fig. 3. Total output RF power for coaxial vircator in Fig. 1.

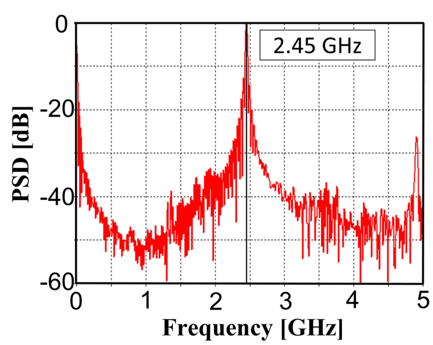

Fig. 4. Power spectral density of the coaxial vircator output power in Fig. 1.

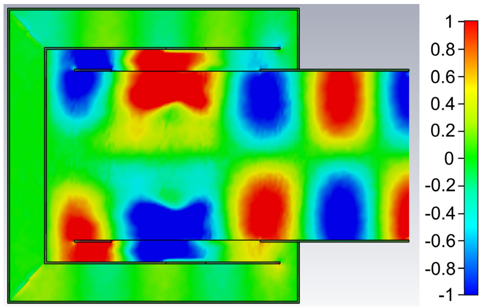

Fig. 5. Normalized *y*-component of the electric field at 2.45 GHz. One notes the zero along the *z*-axis and the phase inversion in the radial direction, TM_{01} mode characteristics.

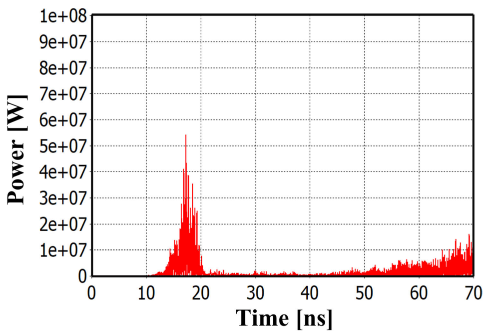

Fig. 6. TE_{11} mode output RF power for coaxial vircator in Fig. 1.

TABLE I
VIRCATOR SIMULATION RESULTS FOR TM_{01}

Parameters	Values
Voltage	350 kV
Absorbed current	27.75 kA
R_a	8.5 cm
AK gap	2.2 cm
Peak power	1.57 GW
Average power	664 MW
RMS Power Efficiency	6.8 %
Peak Power Efficiency	16%
Dominant frequency	2.45 GHz
Total cavity volume	22000 cm^3
Power density	71.4 kW/cm^3

on the device application, the coaxial vircator results in a highly compact and strategic device. However, the working mode makes it impractical, requiring high antenna focusing.

The first step for TE_{11} mode optimization in the coaxial vircator is to use the best techniques found in the literature. In Section III, we also profoundly analyze the already-know technique of sectioned emitter (SE). We wanted to investigate something new, starting with the results obtained, as described in Sections IV and V.

III. TE_{11} Optimization in SE Coaxial Vircators

The symmetry of the device justifies the predominance of the TM_{01} mode on the output port; in fact, the TM_{01} is radially symmetrical.

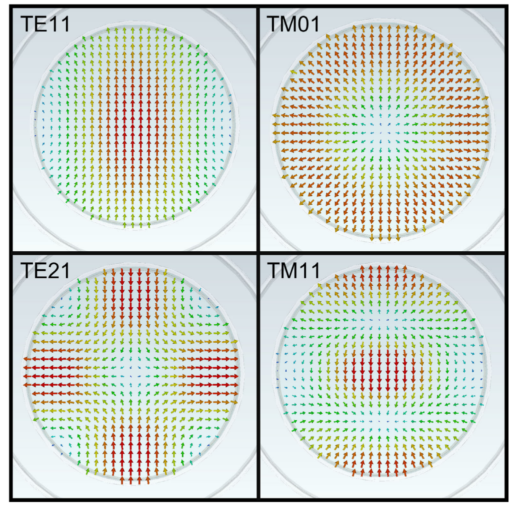

Fig. 7. Electric field pattern of the first four circular waveguide modes.

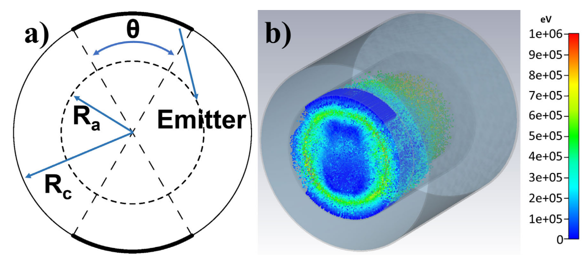

Fig. 8. SE (a) illustration and (b) section of the coaxial vircator with the instantaneous distribution of the electrons during the pulse. The virtual cathode now has a shape that is no longer circular: it concentrates between the two emitters.

Studying the working mode and the electromagnetic field spatial distribution is essential for proper antenna design. The spatial distribution of the electric field of the first four modes in the circular guide is shown in Fig. 7.

The far-field pattern can be obtained by integrating the near fields after the exact current distributions on an antenna are determined by solving the complete boundary value problem of the EM theory [32], [33]. The TM_{01} mode pattern is not optimal when energy is to be focused using a classic horn antenna because the maximum of the far-field is not on the axis of the aperture. For this reason, the TE_{11} mode is preferred [34]. Before the innovative solution to use an elliptic DT (EDT) that we will show later, a coaxial vircator can be designed to enhance the TE_{11} mode using an SE [18], [34], [35], [36], [37], [38], as shown in Fig. 8.

The emission angle θ is parametric; the optimum value found is $\theta = 45°$. However, it is not enough to change the geometry of the emitter to stimulate the TE_{11} mode correctly; it is also necessary to disadvantage the subsequent modes. We have investigated the behavior of the modes with varying the radius of the DT (R_a), with the results shown in Fig. 9. The cutoff frequency of the modes increases, reducing the radius of the DT. Fig. 9 shows a power decrease of the TE_{21} and TM_{01} modes as R_a decreases while the TE_{11} mode increases.

To disadvantage the TM_{01} mode, for the case of the SE coaxial vircator under analysis, we have found the solution to add a short circuit termination (SCT) at the end of DT [18],

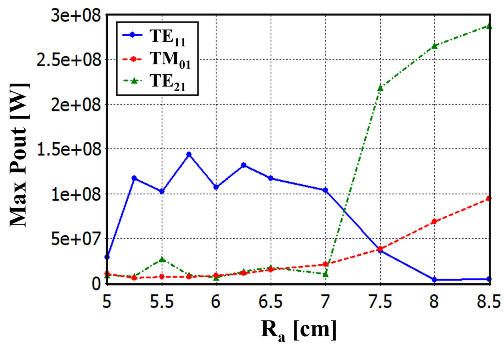

Fig. 9. Output RF power of the TE_{11} (solid line), TM_{01} (dashed line), and TE_{21} (dashed-dotted line) modes as a function of the DT radius.

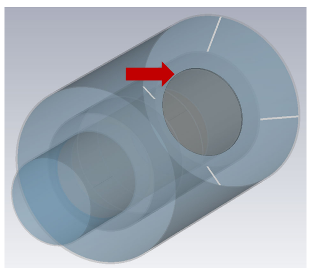

Fig. 10. SCT of the DT.

TABLE II
OBTAINED VALUES FOR AN OPTIMIZED TE_{11} SE COAXIAL VIRCATOR

Parameters	Values
Voltage	350 kV
Absorbed current	16 kA
R_a	5.75 cm
AK gap	2 cm
Peak Power	250 MW
Average power	140 MW
RMS Power Efficiency	2.5 %
Peak Power Efficiency	4.4%
Dominant frequency	2.6 GHz
Total cavity volume	15000 cm^3
Power density	16.7 kW/cm^3

as shown in Fig. 10 with the red arrow. The SCT guarantees the TE_{11} mode the proper load and allows the mode to propagate. The SCT detaches the boundary condition relationship between the generated mode and cathode wall [17]; thus, the axial anode–cathode distance can be arbitrary. The optimization and changes to the coaxial vircator have allowed us to obtain the results shown in Table II.

The optimization resulted in a substantial increase in TE_{11} mode efficiency and a reduction in volume.

A coaxial vircator in [34] and [35] optimized for the TE_{11} mode has been studied. We reproduced and simulated this device on the 3-D PIC CST Studio Suite. From the simulation conducted, we obtained remarkably comparable results to those reported in the literature, such as, for example, the peak

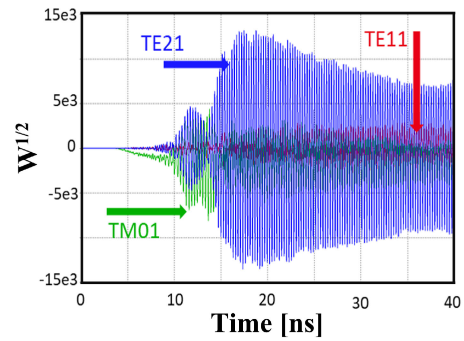

Fig. 11. Output modes in the reproduced device.

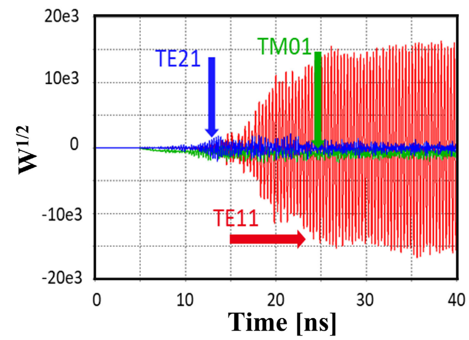

Fig. 12. Output modes in the device presented in this work.

frequency in the spectral power density graph at 3.7 GHz. The lack of some constructive parameters and the nonideality of the actual tested device could bring slight differences with the virtual model we reproduce. However, the design parameters are reported in [35]. Our results are shown in Fig. 11; it is noticed that three modes are present in the output port.

TE_{21} mode appears in simulation; the geometry of the emitter favors this mode considering the pattern of the electric field (see Fig. 7), and it has a cutoff close to that of the TM_{01} mode. In [34], the TE_{21} mode was mentioned, but its presence was excluded only for a geometric hypothesis. The TE_{21} mode pattern does not allow an adequate focus with the classic antennas, such as mentioned for the TM_{01}. In this work, we suppress TE_{21} mode with the SCT technique discussed above. The first three modes obtained in our coaxial vircator are shown in Fig. 12.

From Fig. 12, it is possible to see how the work reported in this article allows for reducing the emission of the TE_{21} mode, thus assigning the maximum output power to the TE_{11}.

In Section IV, we introduce the EDT theory, which is fundamental for the new method we report to further enhance TE_{11} mode in coaxial vircators.

IV. ELLIPTIC CAVITY

The optimization in Section III resulted in a substantial increase in TE_{11} mode. Adding an SCT at the end of DT attenuates the subsequent modes. However, compared with the device optimized for TM_{01} mode, the efficiency of the obtained vircator is less than half. It is due to the presence of unwanted modes, also including degenerate modes. A further step we took to increase the power transfer to the TE_{11} mode: the

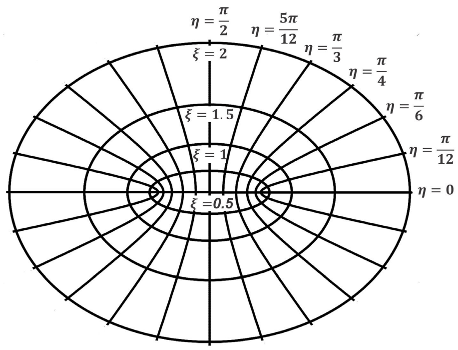

Fig. 13. Confocal elliptic coordinate system.

eccentricity of the DT was changed, making it elliptic in the cross section. Indeed, the elliptical waveguide distinguishes the degenerate modes by changing the cutoff frequencies. In addition, it will enable the fundamental mode to drift away in cutoff frequency from the secondary modes and their degenerate modes.

To evaluate electromagnetic fields in elliptical waveguides, we introduce special functions helpful in studying problems in applied mathematics and physics with elliptic geometries, called Mathieu functions [39], [40]. The computation of Mathieu functions is far from trivial; analyzing these functions is more complex than Bessel functions.

Describing the geometry using confocal elliptical coordinates is convenient, considering an elliptic cross section. In this coordinate system, shown in Fig. 13, we define the angular coordinate η, which represents a set of hyperbolas having the same foci, and the radial coordinate ξ, which gives a set of confocal ellipses. The elliptic variable η has a domain $0 \leq \eta \leq 2\pi$ and plays a similar role to an angular variable in polar coordinates. The variable ξ, in the domain $0 \leq \xi < \infty$, behaves like a radial variable. The elliptic coordinate system (z, ξ, η) of Fig. 13 is related to the right-hand Cartesian system by the following equation, where h is the semi-focal length:

$$\begin{aligned} x &= h \cdot \cosh(\xi) \cdot \cos(\eta) \\ y &= h \cdot \sinh(\xi) \cdot \sin(\eta) \\ z &= z. \end{aligned} \tag{2}$$

The confocal elliptic cylinder with $\xi = \xi_0$ is assumed to coincide with the inner boundary of the EDT. The major and minor axes of the boundary ellipse are $q \cdot \cosh(\xi_0)$ and $q \cdot \sinh(\xi_0)$, respectively, and its eccentricity e is given by $1/\cosh(\xi_0)$.

Considering Maxwell's equations in an elliptical waveguide, is it possible to derive the wave equation for fields E_z for TM modes and H_z for TE modes in an elliptic coordinate system

$$\left[\frac{\partial^2}{\partial \xi^2} + \frac{\partial^2}{\partial \eta^2} + k_c^2 \cdot h^2\left[\sinh^2(\xi) + \sin^2(\eta)\right]\right] \cdot \begin{bmatrix} E_z \\ H_z \end{bmatrix} = 0 \tag{3}$$

where $k_c^2 = k^2 + \gamma^2$, $k^2 = \omega^2 \epsilon \mu - j\omega\mu\sigma$, and $\gamma = \alpha + j\beta$ [41], h is the semi-focal length, and σ is the medium conductivity. μ and ε are, respectively, the medium permeability and permittivity. The considered system has no losses, and the medium is the vacuum.

Two differential equations that coincide with the canonical Mathieu equation (4a) and the modified canonical Mathieu equation (4b) can be obtained by developing the wave equation and separating the independent variables

$$\frac{\mathrm{d}^2}{\mathrm{d}\eta^2} G(\eta) - (a - 2q\cos(2\eta))G(\eta) = 0 \tag{4a}$$

$$\frac{\mathrm{d}^2}{\mathrm{d}\xi^2} F(\xi) - (a - 2q\cosh(2\xi))F(\xi) = 0 \tag{4b}$$

where F and G are the radial and angular functions, respectively, and they represent the electric field and the magnetic field, $q = [(k^2 + \gamma^2) \cdot h^2]/4$, and $a = [(k^2 + \gamma^2) \cdot h^2]/2 + A$, A is the separation constant. In this work, we shall confine our attention to the solutions of the canonical differential (4a) having period π or 2π [40], which is why they can be represented as Fourier series expansions; they are called angular functions. The resulting functions are called "elliptic sine" and "elliptic cosine," $\mathrm{se}_m(\eta, q)$ and $\mathrm{ce}_m(\eta, q)$, where m is the order of the Mathieu functions. The solutions of the modified Mathieu equation, on the other hand, are functions that can be represented by expansions series of Bessel functions; they are called radial functions, denoted by $\mathrm{Rse}_m(\xi, q)$ and $\mathrm{Rce}_m(\xi, q)$. From this point, notations "e" and "o" will distinguish even and odd modes.

We are interested in the behavior of cutoff wavelength values as the eccentricity of the EDT changes, approximating them with a waveguide with an elliptic cross section. Cutoff wavelengths occur when the longitudinal component of the propagation constant k is 0. Considering the boundary conditions for modes TE and TM, the appropriate formal solutions of (3) are, respectively, the following equations for fields along the direction of propagation z:

$$\begin{pmatrix} H_{z,\mathrm{TE}e} \\ H_{z,\mathrm{TE}o} \end{pmatrix} = \begin{pmatrix} \bar{C}_{m,p} \cdot \mathrm{Rce}_m(\xi, q_{m,p}) \cdot \mathrm{ce}_m(\eta, q_{m,p}) \\ \bar{S}_{m,p} \cdot \mathrm{Rse}_m(\xi, \bar{q}_{m,p}) \cdot \mathrm{se}_m(\eta, \bar{q}_{m,p}) \end{pmatrix} \cdot W_p(t, z) \tag{5}$$

$$\begin{pmatrix} E_{z,\mathrm{TE}e} \\ E_{z,\mathrm{TE}o} \end{pmatrix} = \begin{pmatrix} C_{m,r} \cdot \mathrm{Rce}_{\mathrm{m}}(\xi, q_{m,r}) \cdot \mathrm{ce}_m(\eta, q_{m,r}) \\ S_{m,r} \cdot \mathrm{Rse}_m(\xi, \bar{q}_{m,r}) \cdot \mathrm{se}_m(\eta, \bar{q}_{m,r}) \end{pmatrix} \cdot W_p(t, z) \tag{6}$$

where $\bar{C}_{m,p}$, $\bar{S}_{m,p}$, $C_{m,r}$, and $S_{m,r}$ are the arbitrary constants determinable in the usual way [42], and $W_p(t, z) = \cos(\omega t - \beta z)$. E_z is null by boundary condition on the edge of the guide ($\xi = \xi_0$) for TM modes

$$\begin{aligned} \mathrm{Rce}_m(\xi, q_{m,r}) &= 0 \\ \mathrm{Rse}_m(\xi, \bar{q}_{m,r}) &= 0 \end{aligned} \tag{7}$$

where $q_{m,r}$ and $\bar{q}_{m,r}$ are the roots of radial Mathieu functions. TE modes have $E_\eta = 0$ on the edge of the guide (by hypothesis $E_z \equiv 0$). Therefore, the following equation holds:

$$\left(\frac{\mathrm{d}}{\mathrm{d}\xi} H_z\right)_{\xi=\xi_0} = 0 \tag{8}$$

follows that

$$\begin{aligned} \mathrm{Rce}'_m(\xi, q_{m,p}) &= 0 \\ \mathrm{Rse}'_m(\xi, \bar{q}_{m,p}) &= 0 \end{aligned} \tag{9}$$

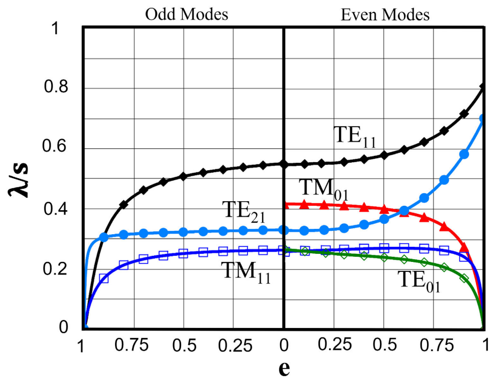

Fig. 14. Relation of normalized cut-off wavelength and the eccentricity.

where $q_{m,p}$ and $\bar{q}_{m,p}$ are the roots of derivatives of radial Mathieu functions. Wavelengths can be obtained from the relation $k_c^2 - \gamma^2 = k^2 = \omega^2 \mu_0 \epsilon_0$, with $\gamma = 0$

$$\lambda_{\text{co}} = \frac{\pi \cdot h}{\sqrt{q_{m,r/p}}} = \frac{\pi \cdot a \cdot e}{\sqrt{q_{m,r/p}}} \tag{10}$$

where a is the length of the major semi-axis and e is the ellipse eccentricity. In confocal elliptical coordinates, the periphery of the waveguide can be derived from the following relation:

$$s_{\text{wg}} = a \cdot \int_0^{2\pi} \sqrt{1 - e^2 \cdot \cos^2 \eta}\, d\eta. \tag{11}$$

The behavior of the cutoff wavelength, normalized for the periphery, is shown in Fig. 14.

For e approaching 0, the even and odd cutoff wavelengths coincide at the same point, equivalent to a circular waveguide cutoff wavelength. For e approaching 1, all modes occur at smaller wavelength values, but the TE_{11e} (even) mode wavelength decreases less. In Fig. 14, TE_{11e} mode appears slightly inversely proportional to (11) because the minor-semi-axis variation poorly affects it. Compared with the evaluations obtained by Chu [39], we also considered the TE_{21} mode, which was not considered before in the literature. The TE_{21e} turns out to have similar behavior to the TE_{11e} mode. The cutoff trend is extremely interesting and exploitable for mode enhancement.

V. Elliptic Coaxial Vircator

The results obtained in Section IV show the isolation of the TE_{11e} and TE_{21e} modes. By combining this behavior with the optimization shown in Section I of this article, it is possible to improve the power transfer to the TE_{11e} mode. The anode, cathode, SCT, and the DT of the coaxial vircator now have an elliptic cross section, as shown in Fig. 15(a). Fig. 15(b) shows the electric field pattern of TE_{11e} mode in the EDT. The chosen emitter is an SE positioned, as shown in Fig. 15(a).

The anode and EDT have parameterized eccentricity. Fig. 16 shows the variation of cutoff frequencies as EDT eccentricity changes; the major-semi-axis length is 5.75 cm. The cathode is designed to keep the anode–cathode distance constant around the perimeter of the anode.

Considering the results in Figs. 14 and 16, the coaxial elliptic vircator was optimized in the eccentricity range of 0.6–0.9. The optimal eccentricity value obtained is 0.8. The variation in cutoff frequencies obtained with the EM simulations is shown in Fig. 16. This variation is consistent with the theoretical results.

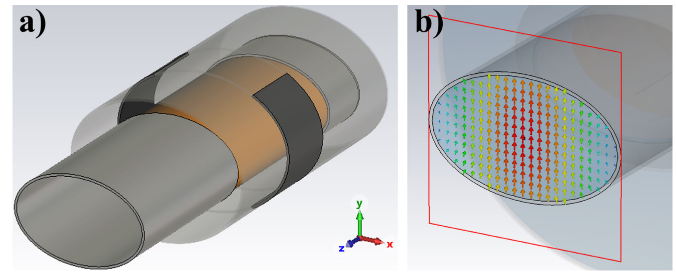

Fig. 15. (a) Anode, cathode, and emitter (red) of a coaxial vircator with elliptic cross section and (b) electric field pattern of the TE_{11e} at the output port, the first mode supported by the elliptical waveguide.

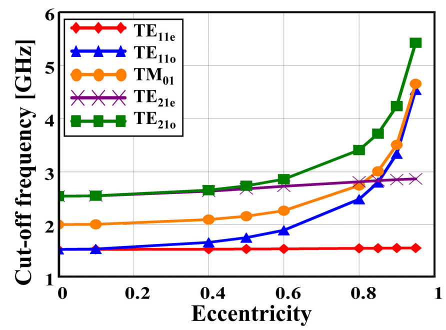

Fig. 16. EDT cutoff frequencies variation in the function of eccentricity.

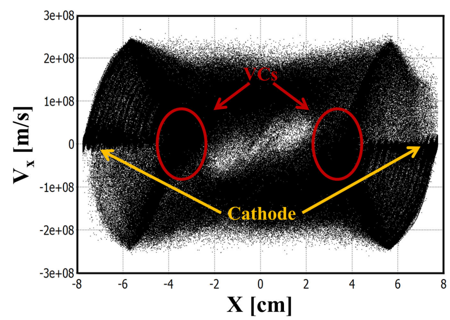

Fig. 17. X-component of velocity in the phase space of beam electrons inside the diode region. Near the emission zone from the SE, distributed along the x-axis, there is the typical eye shape (a shape of electron velocity in phase space that indicates the presence of a virtual cathode) of electron velocity in the diode region, but it is mirrored along the x-axis. So, there are two communicating virtual cathodes.

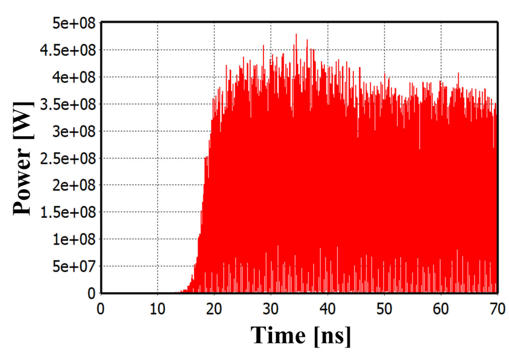

Fig. 18. Total output RF power for elliptic coaxial vircator in Fig. 15.

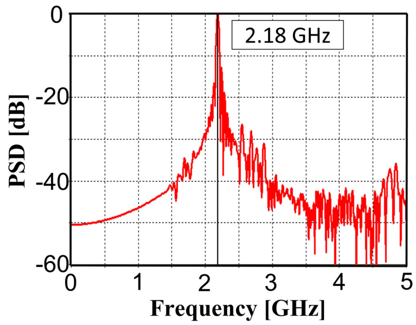

Fig. 19. Power spectral density of elliptic coaxial vircator output power in Fig. 15.

TABLE III
OBTAINED VALUES FOR AN OPTIMIZED TE_{11} ELLIPTIC COAXIAL VIRCATOR

Parameters	Values
Voltage	350 kV
Absorbed current	12.1 kA
EDT major semiaxis	5.75 cm
Eccentricity	0.8
AK gap	2 cm
Peak power	450 MW
Average power	260 MW
RMS Power Efficiency	6.1 %
Peak Power Efficiency	10 %
Dominant frequency	2.18 GHz
Total cavity volume	13000 cm^3
Power density	30.1 kW/cm^3

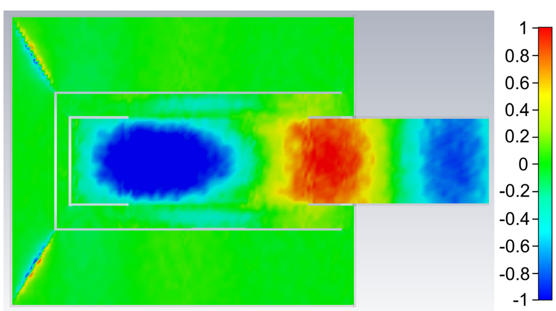

Fig. 20. Normalized y-component of the electric field at 2.18 GHz. One notes the E-field homogeneity inside the DT along the y-axis, which is the TE_{11e} mode characteristic.

PIC simulation was carried out applying the same voltage signal described above; a reduced current of 12.1 kA was found compared with the current of the coaxial vircator optimized for TM_{01}, which was 27.75 kA. Fig. 17 shows the x-component of the velocity in the phase space of electrons in the diode region.

The output power signal in the time domain on the RF output port is shown in Fig. 18, and the spectral power density is shown in Fig. 19. Table III shows the obtained values of the optimized coaxial vircator. The normalized y-component of the electric field at 2.18 GHz, in Fig. 20, shows the predominance of TE_{11e} mode. With the EDT, the coaxial vircator reached an rms power efficiency of 6.1% in the TE_{11e} mode, more than double that of the SE coaxial vircator with a circular cross section.

The power reduction compared to the coaxial vircator optimized for TM_{01} is justified by the decrease in SE for the same emission points. So, it is necessary to size the dynamic load the emitter presents to the source to have the appropriate current [43], [44].

VI. CONCLUSION

The coaxial vircator is a device whose advantages include compactness and simplicity of design. These features make it highly strategic and versatile for military and civil applications. This device naturally works with the TM_{01} mode. The possibility of increasing the power supplied to the TE_{11} mode, necessary for the correct antenna focusing, was investigated. An SE was introduced to improve the TE_{11}, and the DT was modified to disadvantage the other modes. The behavior of mode cutoff frequencies in elliptic guides was studied using Mathieu functions. The cutoff frequencies separate as eccentricity increases. Using elliptic geometry in coaxial vircator resulted in a TE_{11} mode efficiency comparable to that obtained in the device optimized for the TM_{01} mode, with a far more than reduced volume.

REFERENCES

[1] R. Giofrè, P. Colantonio, F. Di Paolo, L. Cabria, and M. Lopez, "Power combining techniques for space-borne GaN SSPA in Ka-band," in *Proc. Int. Workshop Integr. Nonlinear Microw. Millim.-Wave Circuits (INMMiC)*, Jul. 2020, pp. 1–3, doi: 10.1109/INMMiC46721.2020.9160041.

[2] S. Fantauzzi, L. Valletti, and F. Di Paolo, "Virtual prototype of innovative Ka-band power amplifier based on waveguide polarizer," *Adv. Electromagn.*, vol. 9, no. 2, pp. 60–65, Oct. 2020, doi: 10.7716/aem.v9i2.1497.

[3] S. Fantauzzi, L. Valletti, D. Passi, and F. Di Paolo, "An innovative odd-power divider by means of a triple FinLine waveguide to microstrip transition," *Adv. Electromagn.*, vol. 11, no. 1, pp. 58–65, Apr. 2022, doi: 10.7716/aem.v11i1.1742.

[4] L. Valletti, S. Fantauzzi, and F. Di Paolo, "An innovative lens type FinLine to microstrip transition," *J. Infr., Millim., THz Waves*, vol. 43, nos. 7–8, pp. 628–653, Aug. 2022, doi: 10.1007/s10762-022-00869-z.

[5] S. Fantauzzi, L. Valletti, and F. Di Paolo, "High power density spatial combiner for the *Q*-band, ready for space applications," *Prog. Electromagn. Res. M*, vol. 109, pp. 163–177, 2022, doi: 10.2528/PIERM21120903.

[6] D. Passi, A. Leggieri, F. Di Paolo, A. Tafuto, and M. Bartocci, "Spatial power combiner technology," in *Proc. Prog. Electromagn. Res. Symp.*, 2015, pp. 932–938.

[7] D. Passi, A. Leggieri, F. Di Paolo, M. Bartocci, and A. Tafuto, "Design of high power density amplifiers: Application to Ka band," *J. Infr., Millim., THz Waves*, vol. 38, no. 10, pp. 1252–1263, 2017, doi: 10.1007/s10762-017-0402-1.

[8] J. Benford, J. A. Swegle, and E. Schamiloglu, *High Power Microwaves*. Boca Raton, FL, USA: CRC Press, 2015, doi: 10.1201/b19681.

[9] S. Adee, "Portable E-bomb to be tested," *IEEE Spectr.*, Apr. 2009. [Online]. Available: https://spectrum.ieee.org/portable-ebomb-to-be-tested

[10] B. M. Abrams, "The dawn of the e-bomb," *IEEE Spectr.*, vol. 40, no. 11, pp. 24–30, Nov. 2003. [Online]. Available: https://spectrum.ieee.org/the-dawn-of-the-ebomb

[11] W. A. Radasky, "Electromagnetic warfare is here," *IEEE Spectr.*, vol. 51, no. 9, pp. 46–51, Sep. 2014. [Online]. Available: https://spectrum.ieee.org/electromagnetic-warfare-is-here

[12] R. Vadivambal, O. F. Deji, D. S. Jayas, and N. D. G. White, "Disinfestation of stored corn using microwave energy," *Agricult. Biol. J. North Amer.*, vol. 1, no. 1, pp. 18–26, 2010.

[13] C. Gautam, S. K. M. Islam, S. Sadistap, and U. Sarma, "Effect of microwave heat on the nutritional properties of infected red kidney beans," *IEEE Access*, vol. 6, pp. 57137–57143, 2018, doi: 10.1109/ACCESS.2018.2873573.

[14] A. Leggieri, D. Passi, and F. Di Paolo, "Multiphysics modeling based design of a key-holes magnetron," in *Proc. Int. Conf. Numer. Electromagn. Model. Optim. RF, Microw., THz Appl. (NEMO)*, May 2014, pp. 1–4, doi: 10.1109/NEMO.2014.6995658.

[15] A. Leggieri, D. Passi, F. Di Paolo, B. Spataro, and E. Dyunin, "Design of a sub-millimetric electron gun with analysis of thermomechanical effects on beam dynamics," *Vacuum*, vol. 122, pp. 103–116, Dec. 2015, doi: 10.1016/j.vacuum.2015.09.013.

[16] B. M. Kovalchuk, S. D. Polevin, R. V. Tsygankov, and A. A. Zherlitsyn, "S-band coaxial vircator with electron beam premodulation based on compact linear transformer driver," *IEEE Trans. Plasma Sci.*, vol. 38, no. 10, pp. 2819–2824, Oct. 2010, doi: 10.1109/TPS.2010.2060367.

[17] D. Biswas and R. Kumar, "Sensitive dependence of efficiency on cathode-wall position in a coaxial vircator—Numerical studies," *IEEE Trans. Plasma Sci.*, vol. 39, no. 7, pp. 1573–1576, Jul. 2011, doi: 10.1109/TPS.2011.2146792.

[18] Q. Xing, J. Wu, S. Zheng, and C. Tang, "Mode analysis of high-power microwave generation in the inward-emitting coaxial vircator based on computer simulation," *IEEE Trans. Plasma Sci.*, vol. 37, no. 2, pp. 298–303, Feb. 2009, doi: 10.1109/TPS.2008.2009939.

[19] H. Shao, G. Z. Liu, Y. P. Zhang, Z. F. Yang, J. Sun, and Y. C. Zhang, "HPM generation by tri-anode coaxial vircator," *Acta Phys. Polonica A*, vol. 115, no. 6, pp. 1047–1049, Jun. 2009, doi: 10.12693/APhysPolA.115.1047.

[20] S. Mumtaz, H. Uhm, J. S. Lim, and E. H. Choi, "Output-power enhancement of vircator based on second virtual cathode formed by wall charge on a dielectric reflector," *IEEE Trans. Electron Devices*, vol. 69, no. 4, pp. 2043–2050, Apr. 2022, doi: 10.1109/TED.2022.3149455.

[21] S. Mumtaz and E. H. Choi, "An efficient vircator with high output power and less drifting electron loss by forming multivirtual cathodes," *IEEE Electron Device Lett.*, vol. 43, no. 10, pp. 1756–1759, Oct. 2022, doi: 10.1109/LED.2022.3200395.

[22] L. Valletti et al., "Vircator technologies comparison and novel anode analysis," in *Proc. Photon. Electromagn. Res. Symp. (PIERS)*, Nov. 2021, pp. 2781–2789, doi: 10.1109/PIERS53385.2021.9694817.

[23] Q. Xing, D. Wang, F. Huang, and J. Deng, "Two-dimensional theoretical analysis of the dominant frequency in the inward-emitting coaxial vircator," *IEEE Trans. Plasma Sci.*, vol. 34, no. 3, pp. 584–589, Jun. 2006, doi: 10.1109/TPS.2006.875762.

[24] S. Tuan and S. S. M. Chung, "The effects of anode foil transmission ratio on the performance of vircator," in *Proc. 12th Int. Symp. Antennas, Propag. EM Theory (ISAPE)*, Dec. 2018, pp. 1–4, doi: 10.1109/ISAPE.2018.8634356.

[25] J. Walter, J. Vara, C. Lynn, J. Dickens, A. Neuber, and M. Kristiansen, "Initial anode optimization for a compact sealed tube vircator," in *Proc. IEEE Pulsed Power Conf.*, Jun. 2011, pp. 807–810, doi: 10.1109/PPC.2011.6191517.

[26] B. Denny, J. Hammond, and C. Leach, "Full 3-D simulation and optimization of gigawatt class *C*-band 20% efficient coaxial vircator," *IEEE Trans. Electron Devices*, vol. 68, no. 9, pp. 4687–4691, Sep. 2021, doi: 10.1109/TED.2021.3095834.

[27] J. Benford, J. A. Swegle, and E. Schamiloglu, *High Power Microwaves*. Boca Raton, FL, USA: CRC Press, 2015, doi: 10.1201/b19681.

[28] C. Lynn, A. Neuber, E. Matthews, J. Walter, and M. Kristiansen, "A low impedance 500 kV 2.7 kJ Marx generator as testbed for vacuum diodes," in *Proc. IEEE Int. Power Modulator High Voltage Conf. (IPMHVC)*, May 2010, pp. 417–420, doi: 10.1109/IPMHVC.2010.5958383.

[29] P. Appelgren et al., "Study of a compact HPM system with a reflex triode and a Marx generator," *IEEE Trans. Plasma Sci.*, vol. 34, no. 5, pp. 1796–1805, Oct. 2006, doi: 10.1109/TPS.2006.881889.

[30] J. Walter, J. Dickens, and M. Kristiansen, "Performance of a compact triode vircator and Marx generator system," in *Proc. IEEE Pulsed Power Conf.*, Jun. 2009, pp. 133–137, doi: 10.1109/PPC.2009.5386184.

[31] A. A. Neuber, Y. J. Chen, J. C. Dickens, and M. Kristiansen, "A compact, repetitive, 500 kV, 500 J, Marx generator," in *Proc. IEEE Pulsed Power Conf.*, Jun. 2005, pp. 1203–1206, doi: 10.1109/PPC.2005.300570.

[32] C. A. Balanis, *Antenna Theory: Analysis and Design*, 4th ed. Hoboken, NJ, USA: Wiley, 2016.

[33] M.-C. Lin and K.-H. Huang, "Output analysis of a coaxial virtual cathode oscillator [vircator]," in *Proc. 5th IEEE Int. Vac. Electron. Conf.*, Apr. 2004, pp. 182–183, doi: 10.1109/IVELEC.2004.1316262.

[34] C. Moller, M. Elfsberg, T. Hurtig, A. Larsson, and S. E. Nyholm, "Proof of principle experiments on direct generation of the TE_{11} mode in a coaxial vircator," *IEEE Trans. Plasma Sci.*, vol. 38, no. 1, pp. 26–31, Jan. 2010, doi: 10.1109/TPS.2009.2035502.

[35] M. Elfsberg, T. Hurtig, C. Moller, and S. E. Nyholm, "Experimental studies on a coaxial vircator, designed for operation in TE_{11} mode," in *Proc. IEEE Pulsed Power Conf.*, Jun. 2011, pp. 811–814, doi: 10.1109/PPC.2011.6191518.

[36] M. Elfsberg, M. Akyuz, C. Moller, and T. Hurtig, "Optimization study with respect to the point of excitation in coaxial TE_{11} vircator," in *Int. Pulsed Power Conf. Dig. Tech. Paper*, 2013, pp. 3–6, doi: 10.1109/PPC.2013.6627671.

[37] C. Müller, T. Hurtig, A. Larsson, and S. E. Nyholm, "Numerical simulation of direct exitation of the TE_{11} mode in a coaxial vircator," *IEEJ Trans. Fundam. Mater.*, vol. 127, no. 11, pp. 687–692, 2007, doi: 10.1541/ieejfms.127.687.

[38] H. Shao, G. Z. Liu, and Z. F. Yang, "High efficient TE_{11} mode enhanced coaxial vircator," *High Power Laser Part. Beams*, vol. 18, no. 2, pp. 230–234, 2006.

[39] L. J. Chu, "Electromagnetic waves in elliptic hollow pipes of metal," *J. Appl. Phys.*, vol. 9, no. 9, pp. 583–591, Sep. 1938, doi: 10.1063/1.1710459.

[40] N. W. McLachlan, *Theory and Application of Mathieu Functions*, vol. 31, no. 297. London, U.K.: Oxford Univ. Press, 1947.

[41] S. Ramon, J. R. Whinnery, and T. Van Duzer, *Fields and Waves in Communication Electronics*. Hoboken, NJ, USA: Wiley, 1994.

[42] F. Di Paolo, *Networks and Devices Using Planar Transmissions Lines*. Boca Raton, FL, USA: CRC Press, 2000, doi: 10.1201/9781420039689.

[43] Y. Chen, J. Mankowski, J. Walter, M. Kristiansen, and R. Gale, "Cathode and anode optimization in a virtual cathode oscillator," *IEEE Trans. Dielectr. Electr. Insul.*, vol. 14, no. 4, pp. 1037–1044, Aug. 2007, doi: 10.1109/TDEI.2007.4286545.

[44] M. Elfsberg, T. Hurtig, A. Larsson, C. Moller, and S. E. Nyholm, "Experimental studies of anode and cathode materials in a repetitive driven axial vircator," *IEEE Trans. Plasma Sci.*, vol. 36, no. 3, pp. 688–693, Jun. 2008, doi: 10.1109/TPS.2008.922222.

Open Access funding provided by 'Università degli Studi di Roma "Tor Vergata"' within the CRUI CARE Agreement